metals

MDPI

Article

Aging Treatment to Enhance Coercivity Through Grain Boundary Modification in $SmFe_{10}V_2$ Bulk Magnets

Tian-Hong Zhou [1,2], Baochao Zhang [1], Xing Zheng [1], Youngwoon Song [1], Pingzhan Si [1], Chul-Jin Choi [3], Young-Rae Cho [2,*] and Jihoon Park [1,*]

[1] Nano Materials Research Division, Korea Institute of Materials Science, Changwon 51508, Gyeongsangnam-do, Republic of Korea; zhouth@kims.re.kr (T.-H.Z.)
[2] Division of Materials Science and Engineering, Pusan National University, Busan 46241, Republic of Korea
[3] President, Korea Institute of Materials Science, Changwon 51508, Gyeongsangnam-do, Republic of Korea
* Correspondence: yescho@pusan.ac.kr (Y.-R.C.); jpark@kims.re.kr (J.P.)

Abstract: We explored the potential for an aging treatment to achieve high coercivity, of 0.859 MA/m, in a $SmFe_{10}V_2$ alloy with a $ThMn_{12}$-type structure. Bulk magnets were fabricated by sintering ball-milled powders, followed by aging treatment. XRD and SEM analyses revealed that aging treatment promotes the formation of a Sm-rich grain boundary phase with nano-scale thickness. The high Sm content (~60–80 at.%) and low Fe content (~20–30 at.%) in the grain boundary phase led to non-ferromagnetism, enhancing the coercivity by isolating the 1–12 grains and weakening the dipolar interaction between the grains. The aging temperature and duration were optimized to maximize the Sm-rich phase and minimize the soft magnetic $SmFe_2$ phase. This study provides a new fabrication method for $ThMn_{12}$-type magnets and investigates the relationship between microstructure and coercivity, offering valuable insights for the future design and development of high-performance $SmFe_{12}$-based magnets.

Keywords: magnetic properties; $ThMn_{12}$; grain boundary; microstructure; aging treatment

check for updates

Citation: Zhou, T.-H.; Zhang, B.; Zheng, X.; Song, Y.; Si, P.; Choi, C.-J.; Cho, Y.-R.; Park, J. Aging Treatment to Enhance Coercivity Through Grain Boundary Modification in $SmFe_{10}V_2$ Bulk Magnets. *Metals* **2024**, *14*, 1387. https://doi.org/10.3390/met14121387

Academic Editors: Zhongwu Liu, Hongya Yu and Youlin Huang

Received: 31 October 2024
Revised: 26 November 2024
Accepted: 2 December 2024
Published: 3 December 2024

Copyright: © 2024 by the authors. Licensee MDPI, Basel, Switzerland. This article is an open access article distributed under the terms and conditions of the Creative Commons Attribution (CC BY) license (https://creativecommons.org/licenses/by/4.0/).

1. Introduction

$SmFe_{12}$-based compositions are considered promising candidates for next-generation, high-performance permanent magnets due to their theoretical magnetic properties and the use of the low-cost rare-earth element, Sm [1–3]. However, two key challenges hinder the development of $SmFe_{12}$-based magnets with the $ThMn_{12}$ structure (space group *I4/mmm*). These challenges are the instability of the $SmFe_{12}$ binary composition and the low coercivity (H_c) compared to common permanent magnets. To achieve a stable $SmFe_{12}$ phase, it is necessary to introduce stabilizing elements by substituting some Fe atoms. This substitution reduces the formation energy of the $ThMn_{12}$ structure. Among commonly used stabilizing elements, such as Ti, V, Cr, Mo, and Si [4–6], V has been proven to be particularly beneficial in stabilizing the 1–12 phase, while also promoting the formation of a Sm-rich grain boundary phase, which significantly enhances the H_c of the magnet [7–10]. This combination of structural stabilization and H_c improvement makes V a highly attractive element in the design of $SmFe_{12}$-based magnets, potentially overcoming the key challenges and unlocking the high-performance potential of these materials.

According to the study of Palanisamy et al. [11], the ferromagnetic grain boundary phase renders the magnetic decoupling of 1–12 grains impossible, which causes the nucleation of the reversal magnetic domain in a low magnetic field. Therefore, decreasing the content of Fe to form an Fe-lean grain boundary phase is necessary to develop a high H_c. Generally, the Fe-lean grain boundary phase is not a ferromagnetic phase, so it is called the non-ferromagnetic phase. In the Sm-Fe-V system, it has been demonstrated that a three-phase equilibrium exists during heat treatment [12]. The formation of a liquid phase during this process aids in reducing the magnetic coupling of the 1–12 grains in the

final bulk materials, leading to high H_c in $SmFe_{12}$-based bulk magnets. Tozman et al. [13] investigated $Sm(Fe,V)_{12}$ films with a high V content. Two low-melting-point grain boundary phases were identified: a Sm-rich, Fe-lean phase and a V-rich, Fe-lean phase. These phases were shown to enhance the magnetic isolation of 1–12 grains, thereby improving H_c. Schönhöbel et al. [14] successfully fabricated Sm-Fe-(V,Cu) alloys with nanograins using hot compaction and hot deformation techniques. In their work, a Sm-Cu-rich grain boundary phase, with a thickness of 3–6 nm, was formed, resulting in an improved H_c of 0.764 MA/m. Similarly, Zhang et al. [8] explored the Sm-Fe-(Ti,V) system, finding that the non-ferromagnetic Sm-rich grain boundary phase effectively acted as a pinning point, hindering the propagation of magnetic domain walls. This mechanism resulted in a high H_c of 0.796 MA/m. In our previous research [9], Sm-Fe-V alloys were also shown to form a nanometer-scale Sm-rich grain boundary phase, achieving a maximum H_c of 0.844 MA/m with the appropriate Sm content. However, forming this beneficial non-ferromagnetic grain boundary phase requires an excess of Sm in the compound. Unfortunately, during the fabrication process, free Sm phases are prone to oxidation, leading to the formation of SmO and Sm_2O_3 in the sintered bulk, which subsequently reduces magnetization. Conversely, reducing the Sm content leads to the replacement of the Sm-rich grain boundary phase by the ferromagnetic α-Fe phase [9,15]. The α-Fe phase is ineffective at providing magnetic decoupling of the 1–12 grains, resulting in lower H_c [11]. Therefore, a critical challenge in the Sm-Fe-V system is successfully forming the Sm-rich grain boundary phase with a relatively lower Sm content, which is the key to improving the magnetic properties while avoiding oxidation and maintaining high H_c.

In Sm-Co magnets, the typical fabrication method involves performing an aging treatment after the sintering process to form a distinct cellular structure [16,17]. This structure consists of 2:17R (Sm_2Co_{17}, rhombohedral) cell interiors, 1:5H ($SmCo_5$, hexagonal) cell boundary precipitates, and 1:3R ($SmCo_3$, rhombohedral) platelets. The cell boundary precipitates enhance H_c through a pinning mechanism. Similarly, in the Sm-Fe-V system, the oversaturated Sm phase was observed in $SmFe_{10}V_2$ sintered magnets [18]. In this study, we aimed to form a Sm-rich grain boundary phase in the $SmFe_{10}V_2$ alloy using an aging treatment. A lower Sm content was used compared to our previous research [18]. The influence of aging treatment on the phase composition, microstructure, and magnetic properties of the alloy was investigated. The aging temperature and time were optimized to enhance H_c of the bulk magnets, focusing on achieving a better magnetic performance through controlled phase evolution and microstructural refinement during the aging process.

2. Experiments

The $Sm_{1.6}Fe_{10}V_2$ ingots were synthesized via induction melting using high-purity Sm (99.9%), Fe (99.95%), and V (99.9%) pieces. The excess Sm in the chemical formula was intended to compensate for the evaporation and oxidation of Sm and to promote the formation of the Sm-rich grain boundary phase. After melting, the ingots were homogenized at 1000 °C for 20 h in an Ar atmosphere. The homogenized ingots were then crushed through hydrogen decrepitation at 250 °C for 5 h and manually ground into powders smaller than 150 μm. To further reduce the particle size to around 5 μm, ball milling was performed using ZrO_2 balls in a 20:1 weight ratio with the powders. The ball-milled powders were initially pressed under a 0.796 MA/m (10 kOe) magnetic field at a pressure of 400 MPa to form anisotropic low-density green bodies. These green bodies were subsequently pressed again under a higher pressure of 3.5 GPa and sintered at 1140 °C for 30 min under an Ar atmosphere. Following sintering, an aging treatment was applied to encourage the formation of the Sm-rich grain boundary phase, critical for enhancing magnetic properties. The aging temperature and duration were optimized at 720–900 °C for 3–30 h.

X-ray diffraction (XRD, D/Max-2500VL/PC, Rigaku, Tokyo, Japan) with Cu-Kα radiation (λ = 1.5406 Å) was used to investigate the phase composition and crystalline structure. The measuring range of 2θ was from 25 to 80° with a measuring speed of 2°/min. The magnetic properties of the bulk samples were assessed using a vibrating sample mag-

netometer (VSM, MicroSense EZ9, KLA, Santa Clara, CA, USA). The square samples (20~100 mg) with a side length of less than 3 mm were measured under a magnetic field of −1.989–1.989 MA/m (−25–25 kOe) at room temperature. During VSM measurement, the direction of the applied field is parallel to the aligned direction of bulk samples. The thermomagnetic curve was measured from room temperature to 600 °C under a magnetic field of 7.958 kA/m (100 Oe) by a physical properties measurement system (PPMS; EverCool II, Quantum Design, San Diego, CA, USA). Scanning electron microscopy (SEM, JSM-6610LV, JEOL Ltd., Tokyo, Japan) and field emission SEM (FE-SEM, JSM-7800F, JEOL Ltd., Tokyo, Japan) were employed to examine the microstructures. During energy-dispersive X-ray spectroscopy (EDS, Oxford Aztec, JEOL Ltd., Tokyo, Japan) measurement, a spot scan, line scan, and mapping were utilized to analyze the composition of the bulk samples.

3. Experimental Results and Discussion

3.1. Aging Temperature Dependence

Figure 1a presents the XRD patterns of the sintered bulk and aging-treated bulks. Figure 1b is a magnified view of Figure 1a in the range of 27°–41°, providing a clearer observation of the precipitated phase peaks. In the sintered bulk, only two phases were detected: the 1–12 phase and the SmO phase. For the aging-treated bulks, the XRD patterns revealed that at lower aging temperatures, such as 730 °C and 760 °C, the peaks remained similar to those of the sintered bulk. However, once the aging temperature reached 800 °C, peaks corresponding to precipitated phases like $SmFe_2$ and Sm-rich phases became apparent. The intensity of these peaks increased with higher aging temperatures, indicating enhanced precipitation of the secondary phases due to improved Sm diffusion. Importantly, no α-Fe phase was detected throughout the aging process, confirming that the decomposition of the 1–12 phase did not occur during the formation of the secondary phases through aging treatment.

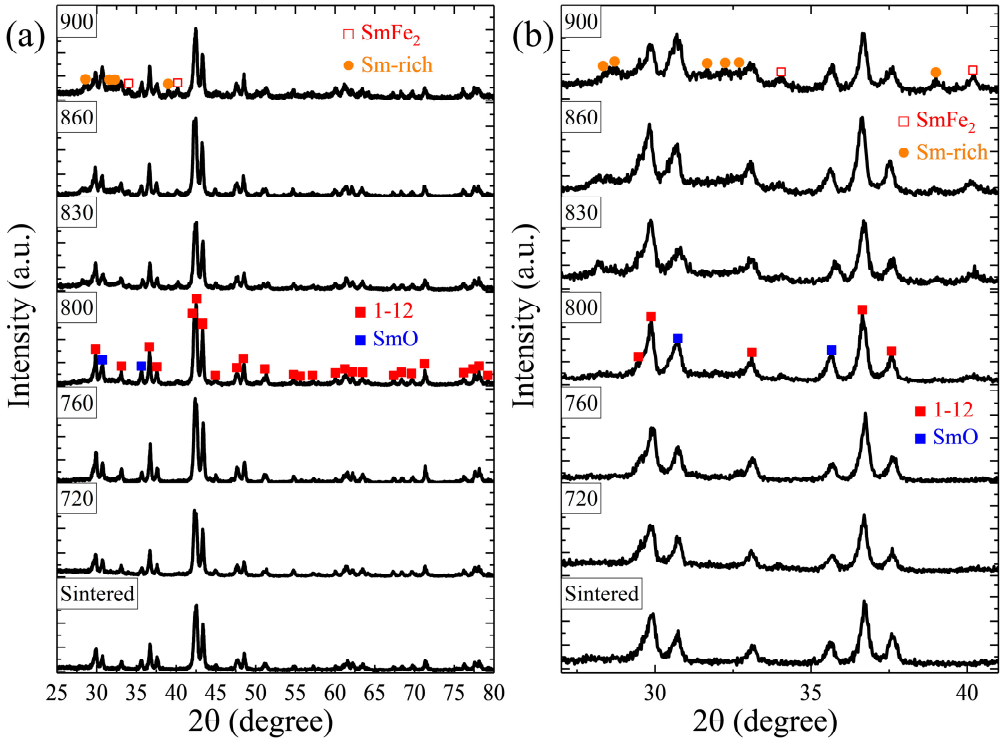

Figure 1. XRD patterns of $SmFe_{10}V_2$ sintered bulk and aging-treated bulks. The aging treatment was performed at 730–900 °C for 10 h. (**b**) Enlarged view of the 27–41° area in figure (**a**).

Figure 2 displays the SEM images of both sintered bulk and aging-treated bulks. In the sintered bulk, two distinct phases were visible in the SEM-BSE image: the gray

phase, identified as the 1–12 phase, and the white phase, identified as SmO, based on EDS analysis. The detailed elemental composition for these phases is presented in Table 1. Interestingly, the Sm content in the 1–12 phase of the sintered bulk was higher than expected, at 7.7 at. %, indicating that Sm is oversaturated in the 1–12 structure. This oversaturation reduced the excess Sm available to form the Sm-rich phase at the grain boundaries of the 1–12 phase, as observed in previous studies [9]. The subsequent images in Figure 2 show the microstructures of aging-treated bulks at various aging temperatures. At temperatures below 800 °C, the diffusion of the Sm element was limited, leading to the slow formation of precipitated phases. Only a few grain boundary phases were detectable. However, when the aging temperature reached 800 °C, a prominent white grain boundary phase appeared among the 1–12 grains. Figure 3a provides a detailed element mapping analysis of the bulk aged at 800 °C, showing distinct regions within the microstructure. The base gray phase is the 1–12 phase, containing Sm, Fe, and V, but no oxygen. EDS analysis (Table 2) reveals that the white phases consist of three types: the SmO phase, with a larger grain size similar to the sintered bulk; the light white Sm-rich phase, which varies in composition between regions I (Sm ~80 at.%) and II (Sm ~70 at.%); and an off-white $SmFe_2$ phase (Sm ~30 at.%). Figure 3b highlights the mapping of the grain boundary phase and the triple junction area in the aging-treated bulk at 800 °C. The line scan in Figure 3b shows the phase on the grain boundary and triple junction area is the Sm-rich phase (Sm~60 at.%, Fe ~32 at.%, V~8 at.%), not the $SmFe_2$ phase. According to the mapping and line scan analysis, the Sm-rich phases are not phases with a fixed composition but are influenced by the diffusion of Sm in the aging treatment. Overall, the grain boundary phase with a Sm-rich and Fe-lean composition effectively isolated the 1–12 grains.

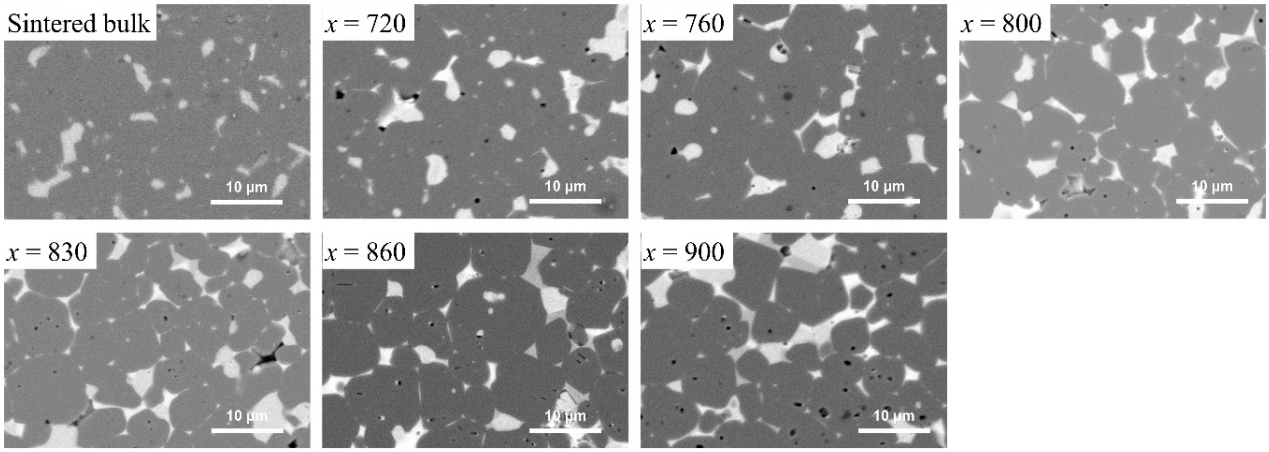

Figure 2. Microstructure of $SmFe_{10}V_2$ sintered bulk and aging-treated bulks. The aging treatment was performed at x °C for 10 h (x = 720–900).

Table 1. EDS data of $SmFe_{10}V_2$ sintered bulk and aging-treated bulks. The regions were chosen from Figure 2. The aging treatment was performed at x °C for 10 h (x = 720–900).

Region		Element (at. %)				Phase
		Sm	Fe	V	O	
Sintering	Gray	8.31	75.17	16.52	-	1–12
	White	48.96	-	3.85	47.19	SmO
x = 720	Gray	7.98	75.30	16.72	-	1–12
x = 760		7.85	76.06	16.09		
x = 800		7.79	75.74	16.37		
x = 830		7.74	75.90	16.36		
x = 860		7.79	75.93	16.28		
x = 900		7.71	76.01	16.28		

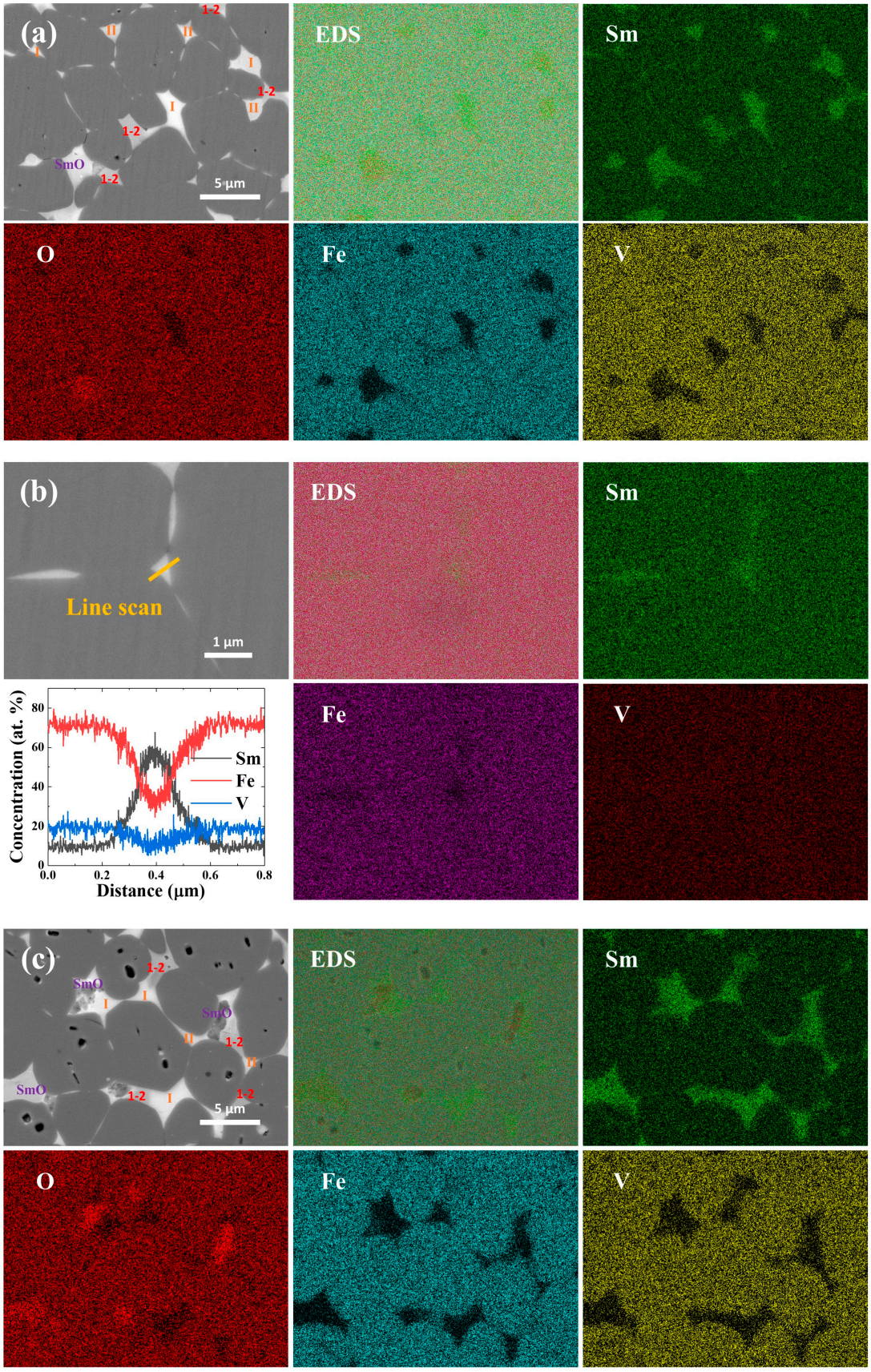

Figure 3. FE-SEM images, related mapping, and line scan of the bulks aging-treated at 800 (**a**,**b**) and 900 °C (**c**) for 10 h.

Table 2. EDS date of $SmFe_{10}V_2$ bulks aging-treated at 800 and 900 °C for 10 h. The regions were chosen from Figure 3.

Aging Temp.	Region	Element (at. %)			
		Sm	Fe	V	O
800 °C	1-2	36.9	63.1	-	-
	I	79.9	15.1	5	-
	II	69.8	30.2	-	-
	SmO	49.3	-	-	50.7
900 °C	1-2	26.8	67.4	5.9	-
	I	77.5	22.5	-	-
	II	42.5	46.3	11.2	-
	SmO	47.6	-	-	52.4

As the aging temperature increased, the grain boundary phase became thicker and, in some cases, developed into the big grains, as can be seen in Figure 2. Concurrently, the ratio of precipitated phases changed. A notable observation was the growth in both content and size of the off-white $SmFe_2$ phase, which began to replace part of the light white Sm-rich grain boundary phase. In Figure 3c, which shows the mapping of the bulk aged at 900 °C, the grain boundary phase is no longer continuous and has diminished in amount. Instead, the Sm-rich and $SmFe_2$ phases have grown significantly in size compared to bulks aged at lower temperatures. When analyzing the precipitated phases, the Sm-rich phase in the bulk aged at 900 °C exhibits a different composition to that at 800 °C, with a reduced Sm content of 46 at.% detected in region II of Figure 3c. The Sm content in the 1–12 phase after aging treatment decreased to 7.7–8.0 at.%, as shown in Table 1. This indicates that during aging, Sm diffused from the 1–12 phase to the grain boundary. The excess Sm in the structure, which caused distortion, diffused and precipitated at the grain boundary to stabilize the 1–12 structure. As the aging temperature increased, accelerated elemental diffusion caused the grain boundary phase to grow in both content and size. Additionally, the higher energy facilitated the formation of the stable $SmFe_2$ phase, which began to dominate over the Sm-rich phase. Another notable effect of aging treatment was the formation of voids, likely due to elemental diffusion and Sm evaporation. The size and number of voids increased with higher aging temperatures, confirming the movement of Sm during the aging process.

Figure 4a,b present the thermomagnetic curve and its derivative of the bulk subjected to aging treatments at 900 °C measured by PPMS. The curve was measured under a magnetic field of 7.958 kA/m. As the temperature increased, the magnetization showed a slow decrease. Before the magnetization dropped to zero, two distinct decreases were observed. The first, larger decrease corresponded to the Curie temperature (T_c) of the 1–12 phase. The second, smaller drop, which brought the magnetization to near zero, was associated with the demagnetization of the $SmFe_2$ phase. As the temperature continued to rise, the magnetization slightly increased due to the minor presence of the α-Fe phase resulting from the decomposition of the 1–12 phase. These curves indicate the absence of other magnetic phases and confirm that the precipitated Sm-rich phase is non-ferromagnetic due to its low Fe content.

The magnetic properties of the sintered and aging-treated bulks were analyzed via hysteresis loops, as shown in Figure 4c. The calculated trends of magnetization and H_c are summarized in Figure 4d. For the sintered bulk, H_c is relatively low at 0.406 MA/m, primarily due to the absence of the Sm-rich grain boundary phase. The excess Sm was lost through evaporation, oxidation, and oversolution in the 1–12 structure, reducing the effectiveness of the magnetic decoupling mechanism. After the aging treatment, H_c showed significant improvement. H_c exhibited a distinct trend with respect to aging temperature, initially increasing and then decreasing. The highest H_c, 0.859 MA/m, was achieved at an aging temperature of 800 °C. Microstructural analysis from Figure 1, Figure 2 amd Figure 3 revealed that the aging process promoted the formation of the Sm-rich grain

boundary phase, which was crucial for enhancing H_c. Up to 800 °C, the grain boundary phase content increased, with most of it being Sm-rich. The thermomagnetic curves in Figure 4a,b confirmed that the Sm-rich phase was non-ferromagnetic, which facilitated the magnetic decoupling of 1–12 grains by preventing the propagation of magnetic domain walls [19]. However, when the aging temperature exceeded 800 °C, H_c began to decline. Although more precipitated phases appeared at higher temperatures, the grain boundary phases became less continuous, and a significant portion of the Sm-rich phase was replaced by the $SmFe_2$ phase. Since $SmFe_2$ is a soft magnetic phase at room temperature [20], it negatively impacted the magnetic decoupling, instead reinforcing the magnetic coupling. The presence of the $SmFe_2$ phase caused a distinct "kink" in the hysteresis loops of the bulks aged above 800 °C, indicative of the detrimental influence of the soft magnetic phase during demagnetization [21]. M_s and M_r were also significantly affected by the precipitated phases. M_s decreased consistently with the increase in precipitated phases. The non-ferromagnetic Sm-rich phase, along with the low-M_s $SmFe_2$ phase, reduced the overall magnetization of the bulks. M_r slightly increased from the sintered bulk to those treated at lower aging temperatures due to the magnetic decoupling effect of the Sm-rich grain boundary phase, which hindered the movement of the domain wall on the grain boundaries. This allowed the bulk to retain higher magnetization after the removal of the external magnetic field. However, at higher aging temperatures, the increased content of precipitated phases, especially the $SmFe_2$ phase, caused a sharp decline in M_r. The $SmFe_2$ phase acted as a nucleation point for reverse magnetic domains, further weakening the magnetic properties. Thus, the presence of the low magnetization phases and the role of $SmFe_2$ in domain reversal significantly lowered the remanence in the bulks subjected to high-temperature aging treatments.

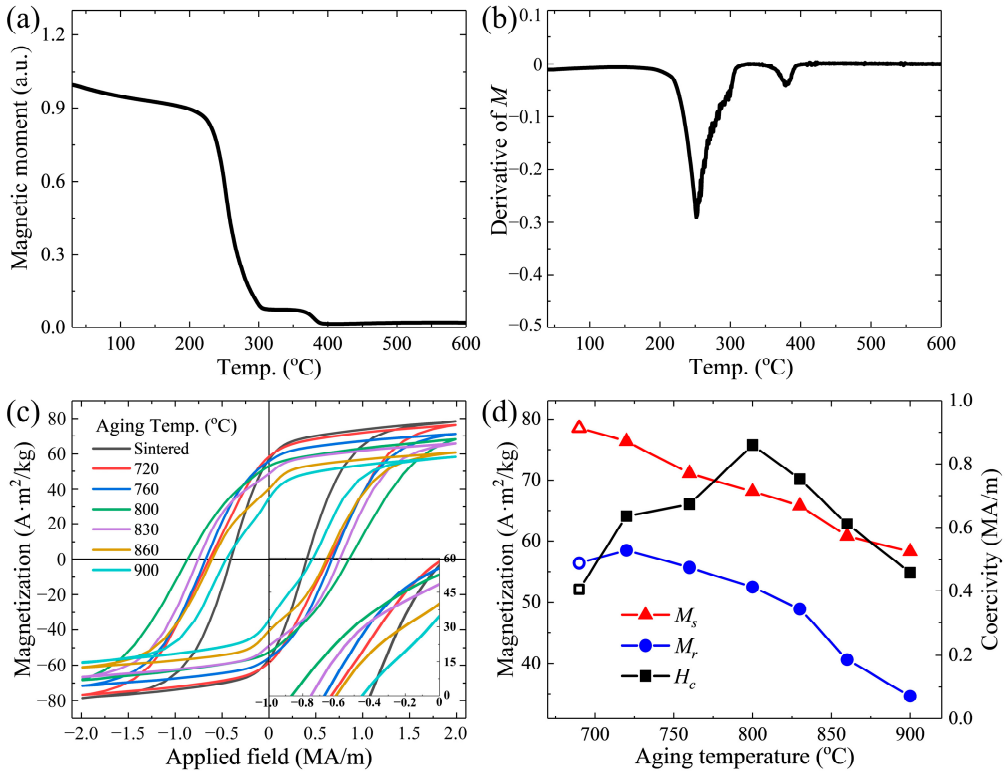

Figure 4. Thermomagnetic curve (**a**) and its derivative (**b**), hysteresis loops (**c**), and M/H-T (**d**) curves of $SmFe_{10}V_2$ sintered bulk and aging-treated bulks. The aging treatment was performed at 730–900 °C for 10 h. The magnetic properties of sintered bulk are shown by the open points in Figure (**c**).

3.2. Aging Time Dependence

According to the analysis of the phase, microstructure, and magnetic properties, 800 °C was identified as the optimal aging temperature, yielding the highest H_c due to the formation of the Sm-rich grain boundary phase. Next, the influence of aging time on these properties was investigated.

Figure 5a presents the XRD patterns of bulks aged at 800 °C for different durations, ranging from 3 to 30 h. Across all samples, the peaks corresponding to the Sm-rich phase were too weak to be clearly distinguished. However, the $SmFe_2$ phase was detectable in the bulks when the aging time exceeded 3 h. Unlike the continuous increase in secondary phases with rising temperature, the intensity of these peaks remained low after 5 h of aging, indicating that the precipitation of secondary phases did not continuously increase with a prolonged aging duration. The SEM images in Figure 5b complement the XRD analysis. For shorter or prolonged aging times, the content of precipitated phases remained minimal. As the aging duration increased from 3 to 10 h, the precipitation of the white grain boundary phase grew more pronounced. In the samples aged for 10 and 15 h, the gray 1–12 grains were effectively separated by the white Sm-rich or $SmFe_2$ phases, suggesting that the grain boundary phase had formed properly. However, for samples aged 20 and 30 h, the content of precipitated phases decreased, and most of the remaining white grains were isolated SmO phases. The XRD patterns confirmed that the $SmFe_2$ phase persisted in these samples, but much of the Sm-rich grain boundary phase had disappeared. The residual grain boundary phase mainly consisted of the $SmFe_2$ phase. This reduction in the Sm-rich grain boundary phase is attributed to the heavy diffusion and evaporation of Sm during long-duration aging treatments, which depleted the excess Sm necessary for maintaining the grain boundary phase. The presence of voids in the bulk material further supported this conclusion. As the aging duration increased, more Sm diffused to the surface and evaporated, resulting in the formation of more voids within the bulk. This loss of Sm content led to the early disappearance of the Sm-rich grain boundary phase, negatively impacting the microstructure and magnetic properties.

The magnetic properties of the bulk samples aged at 800 °C for durations ranging from 3 to 30 h were analyzed using a VSM. The hysteresis loops of the bulks, shown in Figure 6a, were used to calculate M_s, M_r, and H_c, which are summarized in Figure 6b. The trend of H_c with aging duration followed a pattern similar to that observed with aging temperature: it initially increased and then decreased. In these bulk samples, H_c was primarily influenced by the content and composition of the grain boundary phase. Based on XRD and SEM analyses, the highest H_c was achieved when the aging duration reached 10 h, as the content of the Sm-rich grain boundary phase had increased. The improved magnetic decoupling, facilitated by the Sm-rich grain boundary phase, enhanced H_c during this period. However, when the aging duration exceeded 15 h, the content of the grain boundary phase decreased, and the Sm-rich phase was increasingly replaced by the more stable $SmFe_2$ phase. This replacement led to a sharp decrease in H_c, as the $SmFe_2$ phase, being ferrimagnetic, is less effective in promoting magnetic decoupling and instead enhances magnetic coupling of the 1–12 grains. In contrast, M_s and M_r exhibited different trends from H_c. The overall magnetization was influenced by the precipitation of phases such as the Sm-rich and $SmFe_2$ phases. As the aging duration increased, the formation of more Sm-rich and $SmFe_2$ phases led to a decline in magnetization due to their low M_s values. However, when the aging duration became too long (above 15 h), the Sm-rich phase began to decrease as a result of Sm evaporation, which caused a slight recovery of magnetization. Despite this partial recovery, the loss of the Sm-rich phase and the presence of $SmFe_2$ limited the potential for further improvement in magnetic properties.

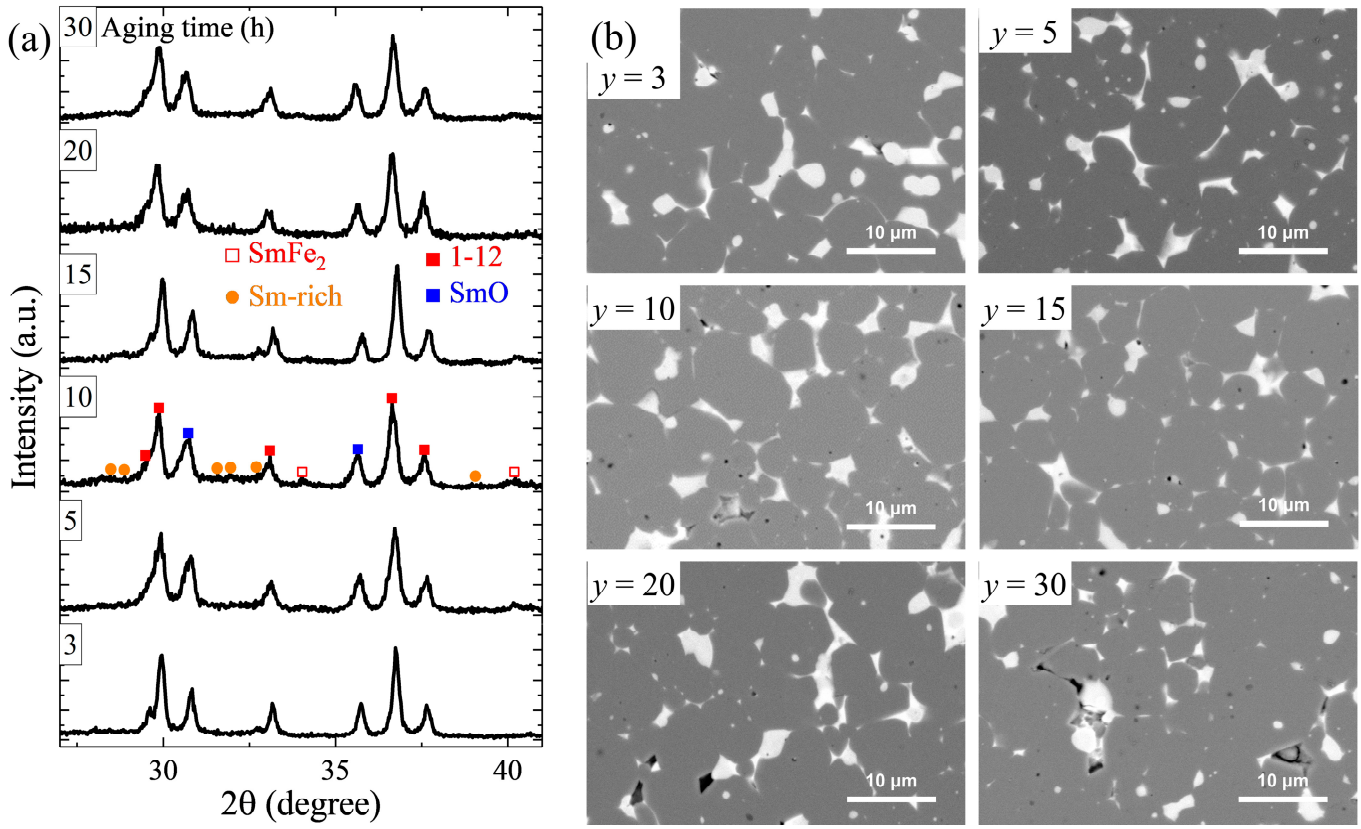

Figure 5. XRD patterns (**a**) and SEM images (**b**) of $SmFe_{10}V_2$ aging-treated bulks. The aging treatment was performed at 800 °C for *y* h (*y* = 3–30).

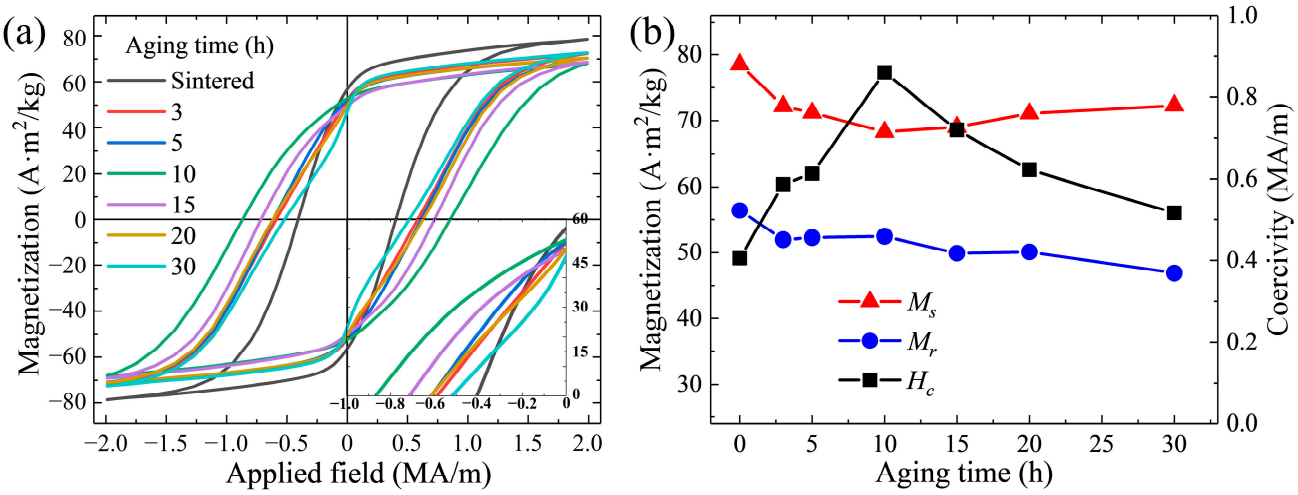

Figure 6. Hysteresis loops (**a**) and *M*/*H*-*t* (**b**) curves of $SmFe_{10}V_2$ sintered bulk and aging-treated bulks. The aging treatment was performed at 800 °C for 3–30 h.

3.3. Discussion of H_c Enhancement Mechanism

The distribution of H_c and magnetic behavior of the sintered and aging-treated samples can be understood through the virgin (initial magnetization curve) and isothermal remanent magnetization (IRM) curves presented in Figure 7a. In the IRM curves, the remanent magnetization was measured after the sample was magnetized at an external magnetic field, by increasing the external magnetic field to obtain a related remanent magnetization. All samples exhibited three distinct magnetization stages in their virgin curves: an initial rapid increase, a slower increase, and a final rapid increase. The first rapid increase

corresponded to reversible magnetization, as indicated by the slow change in M_r observed in the IRM curves. Given that the grain size of the samples (5–10 μm) is much larger than the single domain size of the Sm-Fe-V alloys (0.6–0.75 μm) [8], the movement of the domain wall occurred inside the 1–12 grains and among the 1–12 grains without the Sm-rich grain boundary phases in this stage of the low magnetic field. As the magnetic field increased, the samples entered the second stage, where a slower increase in the virgin curves coincided with an accelerated rise in the IRM curves. In this stage, the movement of the domain walls became pinned by the Sm-rich grain boundary phase and the triple junction areas. When the field reached a level slightly lower than the H_c of the samples, domain walls began to overcome the pinning points, resulting in irreversible magnetization, as can be seen in the accelerated increase in the IRM curves. Finally, the samples transitioned to the third stage, characterized by rapid magnetization due to the domain walls overcoming the pinning phases in the large magnetic field.

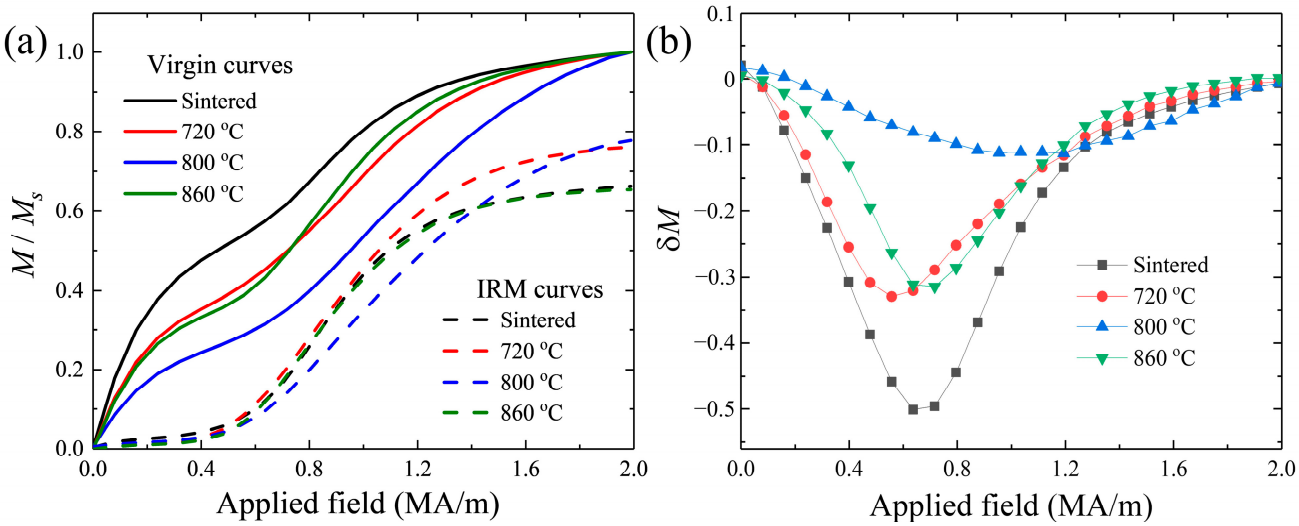

Figure 7. Virgin and IRM curves (**a**) and δM curves (**b**) for the sintered bulk and aging-treated bulks. The aging treatment was performed at 720, 800, and 860 °C for 10 h.

The magnetization behavior of the samples revealed a clear dependence on the aging temperature, as demonstrated by the end values in the first stage of the virgin curves. Among the samples, the one treated at 800 °C showed the lowest value in this stage, indicating reduced reversible magnetization and a higher density of pinning points due to the Sm-rich phases. The microstructural analysis supported this observation, as the content of the Sm-rich grain boundary phase increased up to 800 °C before decreasing at higher temperatures, shown in Figure 2. In the sintered bulks, only thin and minimal Sm-rich grain boundary phases formed [9], which were insufficient for strong domain wall pinning. Following aging treatment, more substantial Sm-rich grain boundary phases isolated the 1–12 grains, enhancing the pinning of domain walls and thereby increasing H_c. However, when the aging temperature exceeded 800 °C, the pinning effect diminished due to a reduction in the Sm-rich phase and an increase in the soft magnetic $SmFe_2$ phase. This led to easier domain wall motion within and among the 1–12 grains, resulting in less effective pinning. A comparison between the samples aged at 720 °C and 860 °C illustrates this temperature effect. While the sample treated at 860 °C exhibited a lower magnetization value in the first stage than the one treated at 720 °C, the slope in the third stage of the 860 °C sample is steeper. This suggests that after higher-temperature aging treatment, the Sm-rich grain boundary phase became more prominent, effectively isolating more 1–12 grains. Consequently, the sample aged at 860 °C was harder to magnetize in low magnetic fields than the sample aged at 720 °C. According to the EDS data in Table 2, the Sm content in the Sm-rich phase decreased with increasing aging temperature. This

reduction in Sm content resulted in a weaker pinning strength. Therefore, in the third stage, where high magnetic fields were applied, the sample aged at 860 °C was magnetized more easily than the one treated at 720 °C. In summary, the overall trend revealed that a higher content of the Sm-rich grain boundary phase and stronger domain wall pinning correlated with a higher H_c. However, excessive aging temperatures reduced the effectiveness of the grain boundary phase and increased the formation of the $SmFe_2$ phase, negatively impacting H_c.

The δM curves (Henkel plots) in Figure 7b assess the magnetic interactions and H_c distribution of the samples by analyzing the IRM and the direct current demagnetization (DCD) curves [22]. In these δM curves, all samples show negative values, indicating the absence of exchange coupling due to the large grain size. This lack of exchange coupling suggested that magnetic grains in the samples interact mainly through dipolar interactions rather than exchange interactions. Among the samples, the sintered bulk exhibits the most negative δM value, reflecting a strong dipolar interaction. The thin and minimal Sm-rich grain boundary phase in this sample failed to effectively isolate the 1–12 grains, leading to strong dipolar interactions of the 1–12 grains. This resulted in a lower H_c, as the dipolar interaction aligned the magnetic moments in an antiparallel fashion, weakening the overall magnetic properties [23,24], like the low M_r/M_s. Aging treatment significantly enhanced the isolation of 1–12 grains by increasing the thickness and content of the Sm-rich grain boundary phase. This reduced the dipolar interactions between the grains, leading to weaker magnetic interactions. As a result, the δM values in the aged samples became less negative compared to the sintered bulk. Notably, the sample aged at 800 °C had a δM value close to zero, and its curve appeared nearly horizontal. This suggested that the Sm-rich grain boundary phase in this sample was optimally developed, providing sufficient isolation of the 1–12 grains and weakening the magnetic interactions. The weak interaction between the grains resulted in enhanced H_c and M_r/M_s.

In this study, we applied aging treatment to $SmFe_{10}V_2$ alloys to investigate its effect on H_c and microstructure. Unlike Sm-Co magnets, where aging treatment forms a cellular structure [25], in $SmFe_{12}$-based magnets, aging treatment promoted the precipitation of a Sm-rich grain boundary phase. Despite similar grain sizes between sintered and aging-treated bulks, H_c significantly increased from 0.406 MA/m in the sintered bulk to 0.859 MA/m in the optimized aging-treated bulk. This suggested that H_c was primarily influenced by the grain boundary phase. Previous studies have shown that without a non-ferromagnetic grain boundary phase, fine grain structures only slightly improve H_c in $SmFe_{12}$-based magnets [26], influenced by the intergrain exchange interaction and the magnetic anisotropy energy [27,28].

A critical question remains: how can a uniform and optimal Sm-rich grain boundary phase be formed in $SmFe_{12}$-based magnets? One challenge is the oxidation of Sm during fabrication, leading to the formation of the SmO phase, as can be seen in Figure 2 and Table 1. This SmO phase depleted Sm from the grain boundary, reducing the formation of the desired Sm-rich phase and impairing its continuity. The non-homogeneously distributed oxides degraded H_c [29]. Future optimization of the fabrication process must aim to minimize Sm oxidation. Although the aging treatment successfully formed Sm-rich grain boundary phases, it also caused the precipitation of the soft magnetic $SmFe_2$ phase, which hindered further improvements in H_c. In Nd-Fe-B magnets, a non-ferromagnetic phase content of around 9.9% is ideal for enhancing H_c [30], implying that a higher content and thicker grain boundary phase are beneficial. To promote more Sm-rich grain boundary phases, the aging temperature and duration must be sufficiently high and long. Optimizing these parameters is crucial to increase the Sm-rich phase without encouraging the formation of $SmFe_2$. Furthermore, reducing the SmO and $SmFe_2$ phases and lowering the content of stabilizing elements like V is necessary to enhance magnetization for practical applications. Overall, this study highlights the potential for achieving high H_c in $SmFe_{12}$-based magnets through precise control of the microstructure, particularly in grain boundary tuning and phase management.

4. Conclusions

In this study, we explored the effects of aging treatment on the microstructure and magnetic properties of Sm-Fe-V alloys. By optimizing the aging process, we successfully fabricated anisotropic bulk magnets with a high H_c of 0.859 MA/m. The aging treatment facilitated the precipitation of Sm-rich and $SmFe_2$ grain boundary phases, crucial for influencing magnetic properties. The optimization of aging temperature and duration proved effective in maximizing the formation of the non-ferromagnetic Sm-rich grain boundary phase, which enhanced magnetic decoupling, while minimizing the presence of the soft magnetic $SmFe_2$ phase that otherwise reduced H_c. According to the analysis of the δM curves, the magnetic decoupling represented the decline in dipolar interaction, which was influenced by the distance of the magnetic grains. Although magnetization slightly decreased due to the precipitation of secondary phases, the overall enhancement of H_c demonstrated the effectiveness of this approach in improving magnetic performance. Through this work, we have introduced a novel method for fabricating $ThMn_{12}$-type magnets with high H_c. Our findings provide valuable insights into the optimization of aging treatments to enhance magnetic properties, offering promising strategies for future material design.

Author Contributions: Conceptualization, T.-H.Z., Y.S. and J.P.; Data Curation, T.-H.Z. and X.Z.; Formal Analysis, T.-H.Z. and B.Z.; Investigation, T.-H.Z., B.Z., Y.S., Y.-R.C. and J.P.; Methodology, T.-H.Z., B.Z. and X.Z.; Project Administration, J.P.; Supervision, C.-J.C., Y.-R.C. and J.P.; Validation, T.-H.Z. and P.S.; Writing—Original Draft, T.-H.Z.; Writing—Review and Editing, P.S., C.-J.C., Y.-R.C. and J.P. All authors have read and agreed to the published version of the manuscript.

Funding: This work was supported by a Korea Institute of Energy Technology Evaluation and Planning (KETEP) grant funded by the Korean Ministry of Trade, Industry and Energy (MOTIE) (No. RS-2023-00237024, Development and demonstration of medium-sized, variable-speed, high-power motor).

Data Availability Statement: The original contributions presented in this study are included in the article. Further inquiries can be directed to the corresponding authors.

Conflicts of Interest: The authors declare no conflicts of interest. The funders had no role in the design of this study; in the collection, analyses, or interpretation of data; in the writing of the manuscript; or in the decision to publish the results.

References

1. Hadjipanayis, G.C.; Gabay, A.M.; Schönhöbel, A.M.; Martín-Cid, A.; Barandiaran, J.M.; Niarchos, D. $ThMn_{12}$-Type Alloys for Permanent Magnets. *Engineering* **2020**, *6*, 141–147. [CrossRef]
2. Gabay, A.M.; Hadjipanayis, G.C. Recent Developments in RFe_{12}-Type Compounds for Permanent Magnets. *Scr. Mater.* **2018**, *154*, 284–288. [CrossRef]
3. Makurenkova, A.; Ogawa, D.; Tozman, P.; Okamoto, S.; Nikitin, S.; Hirosawa, S.; Hono, K.; Takahashi, Y.K. Intrinsic Hard Magnetic Properties of $Sm(Fe,Co)_{12-x}Ti_x$ Compound with ThMn12 Structure. *J. Alloys Compd.* **2021**, *861*, 158477. [CrossRef]
4. Coehoorn, R. Electronic Structure and Magnetism of Transition-Metal-Stabilized $YFe_{12-x}M_x$ Intermetallic Compounds. *Phys. Rev. B* **1990**, *41*, 11790–11797. [CrossRef]
5. De Mooij, D.B.; Buschow, K.H.J. Some Novel Ternary $ThMn_{12}$-Type Compounds. *J. Less Common Met.* **1988**, *136*, 207–215. [CrossRef]
6. Dirba, I.; Harashima, Y.; Sepehri-Amin, H.; Ohkubo, T.; Miyake, T.; Hirosawa, S.; Hono, K. Thermal Decomposition of $ThMn_{12}$-Type Phase and Its Optimum Stabilizing Elements in $SmFe_{12}$-Based Alloys. *J. Alloys Compd.* **2020**, *813*, 152224. [CrossRef]
7. Tozman, P.; Fukazawa, T.; Ogawa, D.; Sepehri-Amin, H.; Bolyachkin, A.; Miyake, T.; Hirosawa, S.; Hono, K.; Takahashi, Y.K. Peculiar Behavior of V on the Curie Temperature and Anisotropy Field of $SmFe_{12-x}V_x$ Compounds. *Acta Mater.* **2022**, *232*, 117928. [CrossRef]
8. Zhang, J.S.; Tang, X.; Sepehri-Amin, H.; Srinithi, A.K.; Ohkubo, T.; Hono, K. Origin of Coercivity in an Anisotropic $Sm(Fe,Ti,V)_{12}$-Based Sintered Magnet. *Acta Mater.* **2021**, *217*, 117161. [CrossRef]
9. Zhou, T.H.; Song, Y.; Zhang, B.; Zheng, X.; Choi, C.-J.; Cho, Y.-R.; Park, J. Enhancing Coercivity through Grain Boundary Phase Modification in $Sm_xFe_{10}V_2$. *J. Mater. Res. Technol.* **2024**, *30*, 3092–3100. [CrossRef]
10. Schönhöbel, A.M.; Madugundo, R.; Gabay, A.M.; Barandiarán, J.M.; Hadjipanayis, G.C. The Sm-Fe-V Based 1:12 Bulk Magnets. *J. Alloys Compd.* **2019**, *791*, 1122–1127. [CrossRef]

11. Palanisamy, D.; Ener, S.; Maccari, F.; Schäfer, L.; Skokov, K.P.; Gutfleisch, O.; Raabe, D.; Gault, B. Grain Boundary Segregation, Phase Formation, and Their Influence on the Coercivity of Rapidly Solidified $SmFe_{11}Ti$ Hard Magnetic Alloys. *Phys. Rev. Mater.* **2020**, *4*, 054404. [CrossRef]
12. Sugimoto, S.; Shimono, T.; Nakamura, H.; Kagotani, T.; Okada, M.; Homma, M. Phase Relation of Sm–Fe–V Alloys around the Compound $Sm_3(Fe,V)_{29}$. *Mater. Trans. JIM* **1996**, *37*, 494–498. [CrossRef]
13. Tozman, P.; Sepehri-Amin, H.; Abe, T.; Hono, K.; Takahashi, Y.K. Exploring Secondary Phases in the Sm–Fe–V System Beneficial for Coercivity. *Acta Mater.* **2023**, *258*, 119197. [CrossRef]
14. Schönhöbel, A.M.; Madugundo, R.; Barandiarán, J.M.; Hadjipanayis, G.C.; Palanisamy, D.; Schwarz, T.; Gault, B.; Raabe, D.; Skokov, K.; Gutfleisch, O.; et al. Nanocrystalline Sm-Based 1:12 Magnets. *Acta Mater.* **2020**, *200*, 652–658. [CrossRef]
15. Zhao, L.; Li, C.; Zhang, X.; Bandaru, S.; Su, K.; Liu, X.; Zhou, Q.; Li, L.; Greneche, J.-M.; Jin, J.; et al. Effects of Sm Content on the Phase Structure, Microstructure and Magnetic Properties of the $Sm_xZr_{0.2}(Fe_{0.8}Co_{0.2})_{11.5}Ti_{0.5}$ (x = 0.8 − 1.4) Alloys. *J. Alloys Compd.* **2020**, *828*, 154428. [CrossRef]
16. Zhou, X.; Liu, Y.; Jia, W.; Song, X.; Xiao, A.; Yuan, T.; Wang, F.; Fan, J.; Ma, T. Revisiting the Pinning Sites in 2:17-Type Sm-Co-Fe-Cu-Zr Permanent Magnets. *J. Rare Earths* **2021**, *39*, 1560–1566. [CrossRef]
17. Dong, C.H.; Wu, H.C.; Liu, L.; Xu, D.S.; Zhou, B.; Sun, Y.L.; Ding, Y.; Liang, J.C.; Yan, A.R. Growth of Defects around Grain Boundary and Evolution of Cellular Structure during Isothermal Aging Process in 2:17-Type SmCo Permanent Magnets. *J. Magn. Magn. Mater.* **2024**, *593*, 171823. [CrossRef]
18. Zhou, T.H.; Zhang, B.; Zheng, X.; Song, Y.; Si, P.; Choi, C.-J.; Cho, Y.-R.; Park, J. Anisotropic $SmFe_{10}V_2$ Bulk Magnets with Enhanced Coercivity via Ball Milling Process. *Nanomaterials* **2024**, *14*, 1329. [CrossRef]
19. Srinithi, A.K.; Tang, X.; Sepehri-Amin, H.; Zhang, J.; Ohkubo, T.; Hono, K. High-Coercivity $SmFe_{12}$-Based Anisotropic Sintered Magnets by Cu Addition. *Acta Mater.* **2023**, *256*, 119111. [CrossRef]
20. Samata, H.; Fujiwara, N.; Nagata, Y.; Uchida, T.; Lan, M.D. Crystal Growth and Magnetic Properties of $SmFe_2$. *Jpn. J. Appl. Phys.* **1998**, *37*, 5544. [CrossRef]
21. Yao, Y.F.; Hou, Y.H.; Li, H.F.; Chai, W.X.; Wu, Z.J.; Feng, Q.; Li, W.; Pang, Z.S.; Ma, L.; Yu, H.B.; et al. Microstructure and Magnetic Properties of Exchange-Coupled Nanocomposite $Sm_{0.75}Zr_{0.25}(Fe_{0.8}Co_{0.2})_{11}Ti$ Alloy. *J. Magn. Magn. Mater.* **2023**, *571*, 170578. [CrossRef]
22. Kelly, P.; O'grady, K.; Mayo, P.; Chantrell, R. Switching Mechanisms in Cobalt-Phosphorus Thin Films. *IEEE Trans. Magn.* **1989**, *25*, 3881–3883. [CrossRef]
23. Vieira, C.; Gomes, R.C.; Silva, F.; Dias, A.; Aquino, R.; Campos, A.; Depeyrot, J. Blocking and Remanence Properties of Weakly and Highly Interactive Cobalt Ferrite Based Nanoparticles. *J. Phys. Condens. Matter* **2019**, *31*, 175801. [CrossRef] [PubMed]
24. García-Otero, J.; Porto, M.; Rivas, J. Henkel Plots of Single-Domain Ferromagnetic Particles. *J. Appl. Phys.* **2000**, *87*, 7376–7381. [CrossRef]
25. Popov, A.G.; Gaviko, V.S.; Popov, V.V.; Golovnia, O.A.; Protasov, A.V.; Gerasimov, E.G.; Ogurtsov, A.V.; Sharin, M.K.; Gopalan, R. Structure and Magnetic Properties of Heat-Resistant $Sm(Co_{0.796-x}Fe_{0.177}Cu_xZr_{0.027})_{6.63}$ Permanent Magnets with High Coercivity. *JOM* **2019**, *71*, 559–566. [CrossRef]
26. Tang, X.; Li, J.; Srinithi, A.K.; Sepehri-Amin, H.; Ohkubo, T.; Hono, K. Role of V on the Coercivity of $SmFe_{12}$-Based Melt-Spun Ribbons Revealed by Machine Learning and Microstructure Characterizations. *Scr. Mater.* **2021**, *200*, 113925. [CrossRef]
27. Bolyachkin, A.S.; Komogortsev, S.V. Power-Law Behavior of Coercivity in Nanocrystalline Magnetic Alloys with Grain-Size Distribution. *Scr. Mater.* **2018**, *152*, 55–58. [CrossRef]
28. Bolyachkin, A.S.; Alekseev, I.V.; Andreev, S.V.; Volegov, A.S. δM Plots of Nanocrystalline Hard Magnetic Alloys. *J. Magn. Magn. Mater.* **2021**, *529*, 167886. [CrossRef]
29. Li, W.F.; Ohkubo, T.; Hono, K.; Sagawa, M. The Origin of Coercivity Decrease in Fine Grained Nd–Fe–B Sintered Magnets. *J. Magn. Magn. Mater.* **2009**, *321*, 1100–1105. [CrossRef]
30. Sasaki, T.T.; Ohkubo, T.; Takada, Y.; Sato, T.; Kato, A.; Kaneko, Y.; Hono, K. Formation of Non-Ferromagnetic Grain Boundary Phase in a Ga-Doped Nd-Rich Nd–Fe–B Sintered Magnet. *Scr. Mater.* **2016**, *113*, 218–221. [CrossRef]

Disclaimer/Publisher's Note: The statements, opinions and data contained in all publications are solely those of the individual author(s) and contributor(s) and not of MDPI and/or the editor(s). MDPI and/or the editor(s) disclaim responsibility for any injury to people or property resulting from any ideas, methods, instructions or products referred to in the content.